Journal of
Materials Chemistry C

ROYAL SOCIETY OF CHEMISTRY

PAPER

View Article Online
View Journal

Cite this: DOI: 10.1039/d5tc04078g

Facilitating rapid ion transport and boosting redox kinetics in Yb/NiCo-LDH for enhanced supercapacitor performance

Shakeel Ahmad,[a] Muhammad Tariq,[a] Longyang Liu,[a] Henmei Ni,*[a] Muhammad Wajid Ullah,[b] Afaq Ullah Khan, *[c] Sameerah I. Al-Saeedi,[d] Zainab M. Almarhoon, [e] Magdi E. A. Zaki[f] and Hassan M. A. Hassan[g]

Received 17th November 2025,
Accepted 28th December 2025

DOI: 10.1039/d5tc04078g

rsc.li/materials-c

A dual atom regulation strategy coupled with anionic defect engineering is shown to be highly effective for tuning the electronic structure and improving the electrochemical behaviour of layered double hydroxides (LDHs). Herein, we present a precisely engineered ytterbium (Yb)-doped NiCo-LDH nanocomposite, where Yb incorporation enables remarkable charge storage capabilities, achieving a high specific capacitance of 2130 F g^{-1} at 1 A g^{-1}. Advanced spectroscopic analysis confirms that the incorporation of Yb dopants induces the formation of oxygen vacancies within the host lattice, which collectively modulate the electronic landscape, facilitating rapid charge propagation and enhanced charge storage mechanism. To assess its practical utility, an asymmetric supercapacitor (ASC) is constructed using Yb_2 as the positive electrode and activated carbon as the negative electrode. Introduction of Yb dopants created additional oxygen vacancies within the LDH lattice, which improved the charge transfer and overall electrochemical performance. The assembled ASC device achieves a high energy density of 78 Wh kg^{-1} at a power density of 751 W kg^{-1} and demonstrates remarkable operational stability, retaining 81% of its initial capacitance after 10 000 cycles at 20 A g^{-1}, with a Coulombic efficiency of 95%. This work establishes a fundamental design principle for next-generation energy storage materials based on synergistic dopant strategies and defect engineering.

1. Introduction

The global energy landscape remains predominantly dependent fossil fuels, which pose environmental risks;[1–6] this, along with the escalating energy demands and proliferation of next-generation renewable technologies intensify the critical need for sustainable alternatives.[7–12] Among the energy storage options, supercapacitors have attracted considerable attention because of their exceptional cycle life and energy storage capability.[13–19] Their operation hinges on two principal mechanisms: pseudocapacitance, which involves surface redox reactions, and electric double layer capacitance, which is produced by the electrostatic charge buildup at the electrode–electrolyte interface.[20–24] The performance of a supercapacitor is largely dictated by the electrode material, driving ongoing efforts to identify compounds with superior electrochemical performance. Supercapacitors are broadly classified into metal/metal oxide-based, carbon material-based, and conductive polymer-based. Notably, layered double hydroxides (LDHs) represent highly promising pseudocapacitive materials due to their inherently large surface area, quasi-two-dimensional (2D) architecture, and considerable interlayer spacing, which promotes swift ion transport.[25–29]

In particular, NiCo-LDH has attracted considerable interest because of the synergistic effect between Ni and Co ions. The presence of multivalent Ni and Co ions enhances the ion exchange capability, improving the overall electrochemical behavior.[30,31] However, the main drawbacks of NiCo-LDH are its relatively low electrical conductivity and the limited number of active sites for redox reactions.[32] To address these

[a] School of Chemistry and Chemical Engineering, Southeast University, Nanjing 211189, PR China. E-mail: henmei_ni@seu.edu.cn
[b] Department of Pulp & Paper Engineering, College of Light Industry and Food Engineering, Nanjing Forestry University, Nanjing 210037, China
[c] School of Chemistry and Chemical Engineering, Jiangsu University, 301 Xuefu Road, Zhenjiang 212013, China. E-mail: afaqchemist@gmail.com
[d] Department of Chemistry, College of Science, Princess Nourah bint Abdulrahman University, P.O. Box 84428, Riyadh 11671, Saudi Arabia
[e] Department of Chemistry, College of Science, King Saud University, P. O. Box 2455, Riyadh-11451, Saudi Arabia
[f] Department of Chemistry, Faculty of Science, Imam Mohammad Ibn Saud Islamic University (IMSIU), Riyadh 11623, Saudi Arabia
[g] Department of Chemistry, College of Science, Jouf University, Sakaka-2014, Saudi Arabia

limitations, element doping has been recognized as an effective approach to create additional oxygen vacancies within the LDH lattice, thereby increasing the number of active sites and improving electrical conductivity.[33] In this context, Wang *et al.* synthesized nitrogen-doped NiCo-LDH, which delivered a specific capacitance of 2193 F g^{-1} at a current density of 1 A g^{-1}, along with 90% capacitance retention after 10 000 charge–discharge cycles.[34] Lei and co-workers fabricated molybdenum-doped NiCo-LDH, achieving an excellent specific capacitance of 1368.4 C g^{-1} with 88% retention after 10 000 cycles.[35] Zan *et al.* prepared manganese-doped NiCo-LDH, which exhibited a high specific capacitance of 4253 F g^{-1} at 1 A g^{-1} and 92% stability after 10 000 charge–discharge cycles.[36] Similarly, Shi and co-workers synthesized sulfur-doped NiCo-LDH, obtaining a specific capacitance of 2417.7 F g^{-1} with 90% capacitance retention after 5000 charge–discharge cycles.[37]

Based on the above discussion, various research groups have introduced different dopants into NiCo-LDH and obtained diverse electrochemical results. In the present study, we synthesized a novel Y/NiCo-LDH composed of porous nanosheets with uniformly distributed pores and multichannel structures using a simple hydrothermal method. The NiCo-LDH synthesized with 0.12 g Yb doping exhibited a porous nanosheet morphology, where the uniformly distributed pores provided a larger surface area and more exposed active sites, leading to enhanced electrochemical activity. The optimized Yb_2 nanocomposite delivered an impressive specific capacitance of 2130 F g^{-1} at a current density of 1 A g^{-1}. Furthermore, the introduction of Yb dopants created additional oxygen vacancies within the LDH lattice, which improved the charge transfer and overall electrochemical performance. The assembled asymmetric supercapacitor (ASC) device, using Yb_2 as the positive electrode and activated carbon as the negative electrode, exhibits an energy storage capability of 78 Wh kg^{-1} and a power output of 751 W kg^{-1}.

2. Experimental

2.1 Chemical reagents

Nickel nitrate hexahydrate ($Ni(NO_3)_2{\cdot}6H_2O$, ≥99%), 2-methylimidazole ($C_4H_6N_2$) (2-mulam), cobalt(II) nitrate hexahydrate ($Co(NO_3)_2{\cdot}6H_2O$), ytterbium(III) nitrate pentahydrate ($Yb(NO_3)_3{\cdot}5H_2O$), urea ($CO(NH_2)_2$), polyvinyl alcohol (PVA), activated carbon, ethanol, and potassium hydroxide, were purchased from Sigma-Aldrich. $Ni(NO_3)_2{\cdot}6H_2O$ and $Co(NO_3)_2{\cdot}6H_2O$ were used as precursors for nickel and cobalt in the synthesis of Yb/NiCoLDH nanocomposites. Ytterbium(III) nitrate pentahydrate provided the Yb ions, and deionized water was used as the solvent for all experimental procedures.

2.2 Synthesis of Yb/NiCoLDH nanocomposites with different Yb ratios

The Yb/NiCo-LDH samples were synthesized using a straightforward hydrothermal protocol. Solution I was prepared by stirring 0.6 g of cobalt(II) nitrate hexahydrate [$Co(NO_3)_2{\cdot}6H_2O$] and 0.3 g of nickel(II) nitrate hexahydrate [$Ni(NO_3)_2{\cdot}6H_2O$] in 40 mL of deionized water. Concurrently, solution II was formed by dissolving 0.633 g of urea and varying amounts of ytterbium nitrate pentahydrate [$Yb(NO_3)_3{\cdot}5H_2O$] (0.0579 g, 0.12 g, and 0.18 g) in 40 mL of deionized water with continuous agitation for 15 minutes. Solution I was then combined with solution II and mixed for an additional 1 hour to ensure homogeneous dispersion. The mixture was transferred to a Teflon-lined stainless-steel autoclave and heated to 120 °C for 8 hours. After cooling to room temperature, the precipitate was collected by centrifugation, washed several times with deionized water and ethanol, and dried at 70 °C under ambient conditions. An undoped NiCo-LDH sample was prepared using the same procedure but without the ytterbium nitrate precursor. The final samples were designated as Yb_0, Yb_1, Yb_2, and Yb_3, corresponding to the progressive incorporation of $Yb(NO_3)_3{\cdot}5H_2O$ amounts of 0, 0.0429, 0.0886, and 0.18 g, respectively. The synthesis workflow is illustrated in Scheme 1.

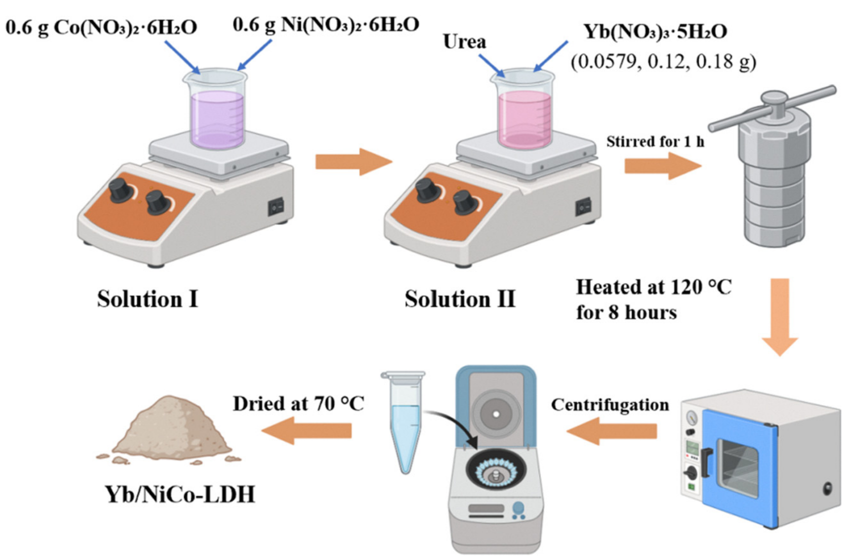

Scheme 1 Schematic of the synthesis of the Yb/NiCo-LDH nanocomposite.

2.3 Synthesis of Yb/NiCoLDH//AC ASC device and its electrochemical measurement

The positive electrode was formed by combining the Yb_2 phase with acetylene black and polyvinylidene fluoride (PVDF) in a weight proportion of 8 : 1 : 1 using *N*-methyl-2-pyrrolidone as the solvent, then applying the resulting slurry to a nickel foam substrate (1.0 cm × 1.0 cm). The negative electrode was produced by utilizing activated carbon as the active material. A CHI660 electrochemical workstation was used to assess the electrochemical performance of the electrode components, including cyclic voltammetry (CV), galvanostatic charge–discharge (GCD), and electrochemical impedance spectroscopy (EIS) measurements. For the gel electrolyte, 1 g of polyvinyl alcohol (PVA) was dissolved in 2 M KOH to yield a clear solution. The positive and negative electrodes were then dipped into this gel electrolyte with a separator positioned between them to assemble the asymmetric supercapacitor (ASC) device. The specific capacitance was calculated from the GCD curves using eqn (1), where I denotes the current density (A g^{-1}), Δt denotes the discharge time, and m is the mass of the active material. The device energy and power densities were calculated using eqn (2) and (3), respectively, where dV is the potential window (V), dt is the discharge duration (s), and C is the specific capacitance.[28]

$$C_F = \frac{(I \times \Delta t)}{m \times \Delta V}, \quad (1)$$

$$E = \frac{(C \times \Delta V^2)}{2 \times 3.6}, \quad (2)$$

$$P = \frac{(E \times 3600)}{\Delta t}. \quad (3)$$

3. Results and discussion

The crystalline structure and phase composition of the synthesized nanocomposites were analyzed using X-ray diffraction (XRD). Fig. 1 presents the XRD profile of the synthesized nanocomposites, which shows diffraction peaks at 2θ positions of 17.23°, 33.72°, 34.80°, 39.42°, 46.85°, and 61.77° correspond to the crystalline planes (003), (110), (012), (015), (009), and (110), respectively, which are attributed to NiCo-LDH according to JCPDS card No. 38-0715. The XRD results indicate that the diffraction peaks of the doped nanocomposites shift slightly towards smaller 2θ positions, suggesting that the introduction of Yb causes lattice distortion in the LDH structure. Additionally, it is observed that as the Yb concentration increases, the intensity of the diffraction peaks decreases, which can be attributed to the distortion induced by Yb in the LDH structure, leading to slight agglomeration of the nanocomposites. Furthermore, to investigate the Yb doping on NiCo-LDH, ICP analysis was performed, as shown in Fig. 1b. The results indicate that Yb was successfully incorporated into the LDH structure. The atomic ratios of the elements are listed in Table 1, showing that in the undoped NiCo-LDH, Co and Ni were present in a 2 : 1 ratio. Moreover, after Yb doping, trace amounts of Yb were detected in the doped samples, and a slight decrease in the Ni and Co ratios was observed. This suggests that Yb partially replaced Ni and Co within the brucite-like structure. The ICP results confirm that Yb was successfully

Table 1 Elemental composition of the synthesized nanocomposites

Sample	Co wt%	Ni wt%	Yb wt%
Yb_0	67	33	0.00
Yb_1	63.98	32.57	3.45
Yb_2	60.02	32.62	7.36
Yb_3	58.18	32.02	9.80

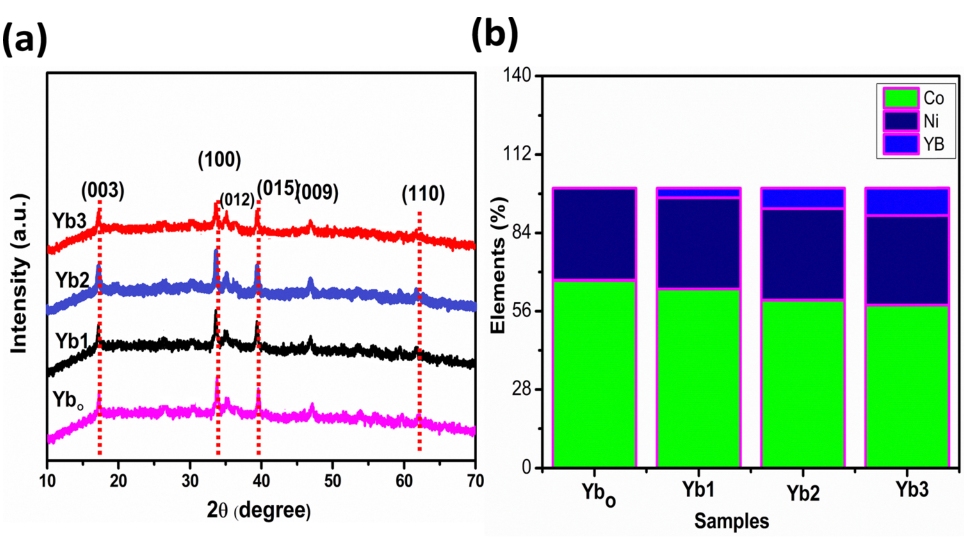

Fig. 1 (a) XRD patterns and (b) ICP results of the synthesized nanocomposites.

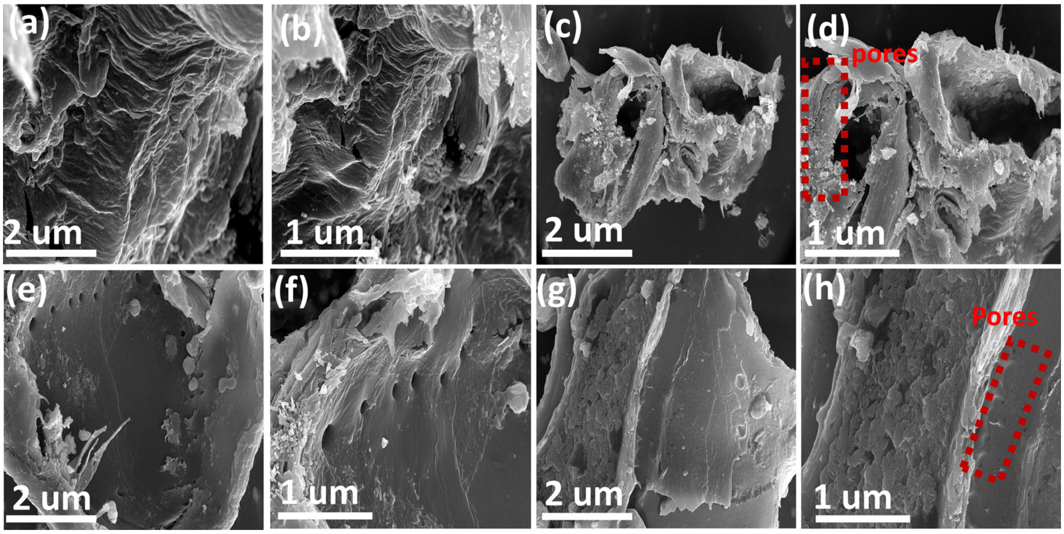

Fig. 2 SEM images of (a) and (b) Yb_0, (c) and (d) Yb_1, (e) and (f) Yb_2, and (g) and (h) Yb_3.

introduced into the NiCo-LDH without disturbing the overall elemental balance.

Scanning electron microscopy (SEM) was used to determine the structural morphology of the synthesized nanocomposites. Fig. 2a and b show the SEM images of NiCo-LDH, indicating that the nanosheets are interconnected with each other and form a wrinkled layered network. Fig. 2c and d present the SEM images of the Yb_1 sample, where the introduction of a small amount of Yb leads to the appearance of small pores on the nanosheets. Furthermore, when a moderate amount of Yb is introduced, the nanosheets become more distinctly porous, and the pore channels are more clearly exposed across the surface, providing a greater number of active sites for electrochemical reactions, as shown in Fig. 2e and f. In contrast, the SEM images of the Yb_3 sample (Fig. 2g and h) show that at higher doping levels, the nanosheets tend to agglomerate due to excessive Yb incorporation, resulting in the loss of the well-defined sheet morphology. It is noted that the SEM morphological observations are consistent with the XRD results. Furthermore, to examine the elemental composition and distribution, EDS mapping was performed. The EDS results confirm that Ni, Co, O, and Yb are uniformly distributed throughout the nanosheets, as shown in Fig. S1 in the SI.

The morphological and crystallographic features of Yb_2 were examined using TEM, HRTEM, and SAED. TEM imaging (Fig. 3a and b) reveals a porous nanosheet architecture for Yb_2, which is consistent with the SEM observations. The HRTEM image shows well-defined lattice fringes with a measured interplanar spacing of 0.67 nm, assignable to the (003) plane of NiCo-LDH, as shown in Fig. 3c. The polycrystalline nature of the material is confirmed by the SAED pattern, shown in Fig. 3e, which exhibits well-defined rings corresponding to the (003), (012), (015), and (110) reflections of NiCo-LDH,[38] aligning with the XRD data and confirming the successful synthesis of the NiCo-LDH phase.

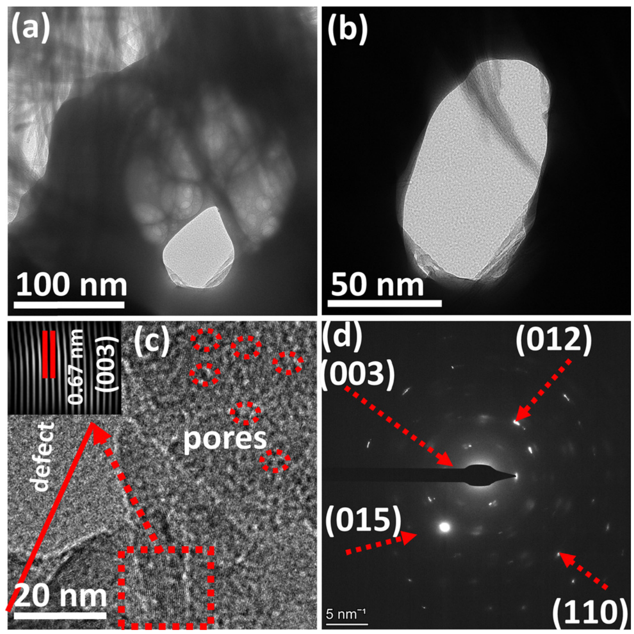

Fig. 3 Characterization of Yb_2: (a) and (b) TEM images at varying magnifications, (c) HRTEM image, and (d) SEAD pattern.

Surface area and porosity were evaluated from nitrogen adsorption–desorption isotherms. The isotherm is classified as type IV with a hysteresis loop observed between relative

Table 2 Surface area and pore size distribution of the synthesized materials

Materials	Surface area (m^2 g^{-1})	Pores size (nm)
Yb_0	130	4
Yb_1	264	6.50
Yb_2	305	8.73
Yb_3	180	5.4

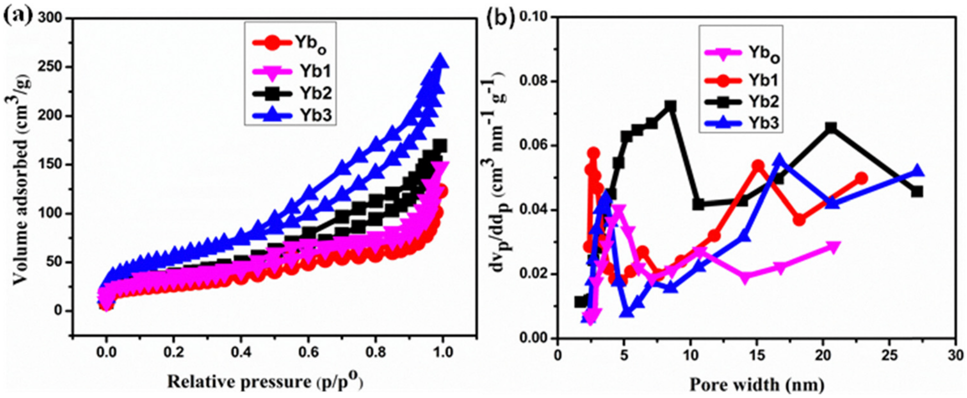

Fig. 4 (a) Nitrogen adsorption–desorption isotherm and (b) BJH pore size distribution of the synthesized materials.

pressures of approximately $0.47 < P/P_0 < 0.943$, signifying a mesoporous architecture beneficial for ion diffusion.[39] The calculated specific surface areas (GA) for Yb_0, Yb_1, Yb_2, and Yb_3 are reported in Table 2, with Yb_2 exhibiting the largest surface area. This enhancement is ascribed to the optimal level of Yb_2 doping, which induces a moderate lattice distortion in the LDH framework and generates additional active sites without compromising structural integrity. Pore size distribution, determined *via* the BJH method and shown in Fig. 4b, spans about 1–30 nm, a range conducive to efficient ion diffusion. Further comparison in Table 2 indicates that Yb_3 possesses noticeably smaller pores, likely resulting from nanosheet aggregation and partial pore collapse that reduces the surface area. In contrast, Yb_2 optimally balances a high surface area with a favorable pore size, yielding an architecture that is favorable for ion transport and superior photocatalytic performance.

The elemental state and composition of the synthesized material were characterized by XPS. The XPS spectra, shown in Fig. 5a, exhibit Ni 2p features with two main components at approximately 855 eV and 874 eV, corresponding to Ni^{2+} and

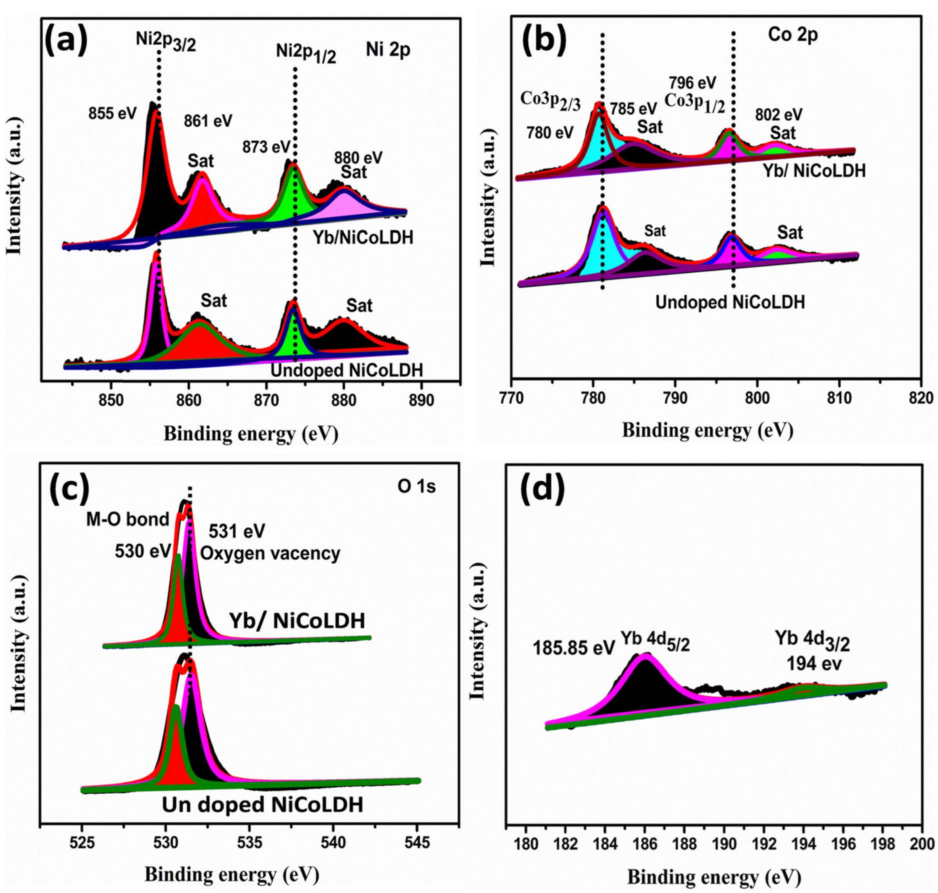

Fig. 5 XPS spectra of (a) Ni 2p, (b) Co 2p, (c) O 1s and (d) Yb 3d.

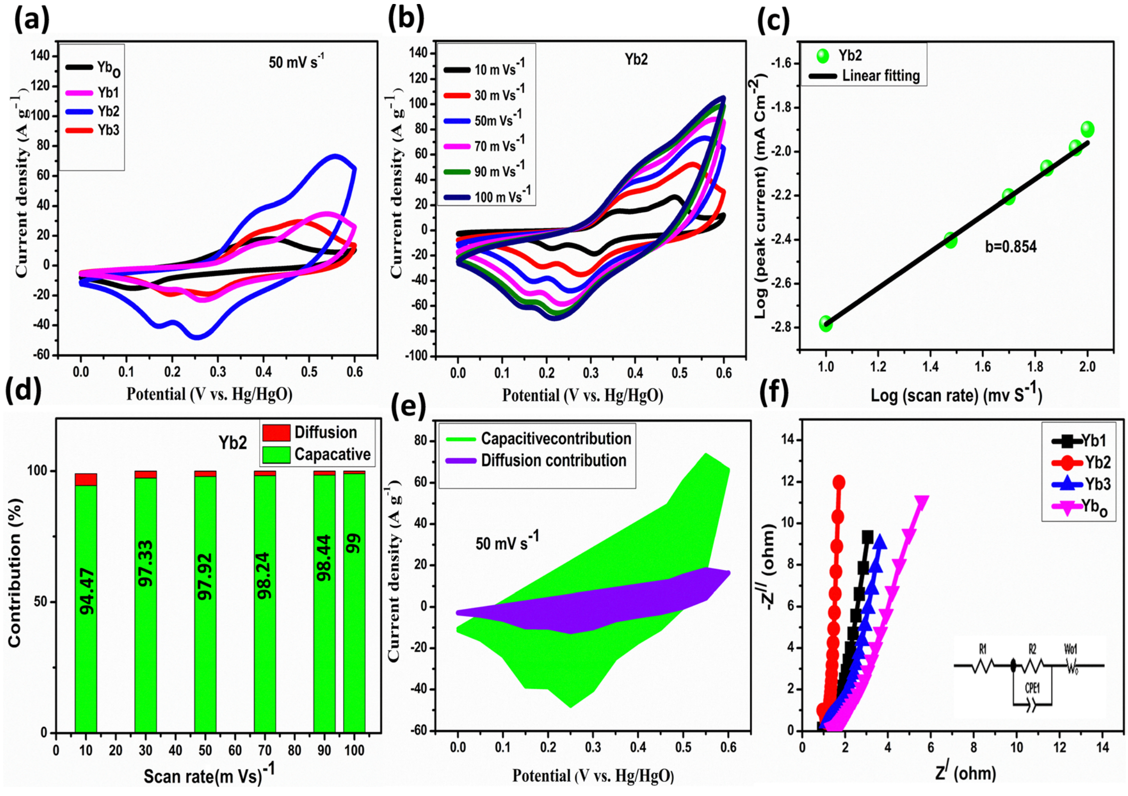

Fig. 6 Electrochemical performance of the NiCoLDH-based materials: (a) CV curves of Yb_0, Yb_1, Yb_2 and Yb_3, and (b) CV curves of Yb_2 at different scan rates. (c) Plots of current (*i*) *versus* scan rate (*V*) of Yb_2. (d) and (e) Capacitive and diffusion contribution ratio of Yb_2. (f) Nyquist plots of the Yb_0, Yb_1, Yb_2 and Yb_3 electrodes.

Ni^{3+} in the Ni $2p_{3/2}$ and Ni $2p_{1/2}$ regions, respectively, along with two satellite features near 861 eV and 881 eV.[40] Similarly, the Co 2p spectrum is deconvoluted into primary peaks at 782 eV and 797 eV, assigned to Co^{3+} and Co^{2+}, with two ancillary satellites at 785 eV and 802 eV,[29] as illustrated in Fig. 5b. The O 1s spectrum includes a peak around 530 eV assigned to the M–O bond and another feature at 531 eV, indicating oxygen vacancies, as displayed in Fig. 5c.[41] Furthermore, the Yb 4d region shown in Fig. 5d contains peaks at 185 eV (Yb $4d_{5/2}$) and 194 eV (Yb $4d_{3/2}$), respectively, confirming the doped Yb state within the nanocomposite matrix.[42]

The electrocatalytic properties of the synthesized materials were assessed in a three-electrode configuration using 2 M KOH electrolyte. Fig. 6a presents the CV for the materials at a scan rate of 50 mV s^{-1}, where the Yb_2 sample shows a notably larger electrochemical area, likely due to increased porosity, enhanced specific surface area, and optimal Yb_2 doping levels. Additionally, the CV profiles for the Yb_2 sample at varying scan rates reveal a pair of redox peaks associated with species such as Ni, Co, and NiCo-LDH, as shown in Fig. 6b.[43,44] The CV curves for Yb_0, Yb_1, and Yb_3, provided in Fig. S2 of the SI, similarly display distinct redox peaks, confirming the reversibility of the redox processes across all samples. The underlying redox mechanisms responsible for this behavior are listed below.[38]

$$\text{Ni (OH)}_2 + \text{OH}^- \leftrightarrow \text{NiOOH} + e^- + H_2O, \quad (4)$$

$$\text{Co (OH)}_2 + \text{OH}^- \leftrightarrow \text{CoOOH} + e^- + H_2O, \quad (5)$$

$$\text{CoOOH} + \text{OH}^- \leftrightarrow \text{CoO}_2 + e^- + H_2O. \quad (6)$$

Furthermore, the following equation were used to examine the capacitive feature and reaction kinetics of the Yb_2.[23]

$$I = av^b, \quad (7)$$

$$\log(i) = \log(a) + b\log(v). \quad (8)$$

The data indicate a slope (*b*) of 0.854, which implies that the composite behaves predominantly in a capacitive manner, given that the *b* value approximates the theoretical ideal of 1.0,[45] as shown in Fig. 6c. Quantitative deconvolution using eqn (9) and (10), with coefficients k_1 and k_2 established from the correlation between $V^{1/2}$ and $i(V)^{1/2}$ display in Fig. 6d and e, revealed that the capacitive contribution for the Yb_2 electrode escalates from 93% to 99% as the scan rate increases from 10 to 100 mV s^{-1}. Consequently, this dominant capacitive process

Table 3 R_s and R_{ct} values of the synthesized nanocomposites

Material	R_s	R_{ct}
Yb_0	0.72	1.13
Yb_1	0.93	1.55
Yb_2	1.08	1.96
Yb_3	1.36	2.13

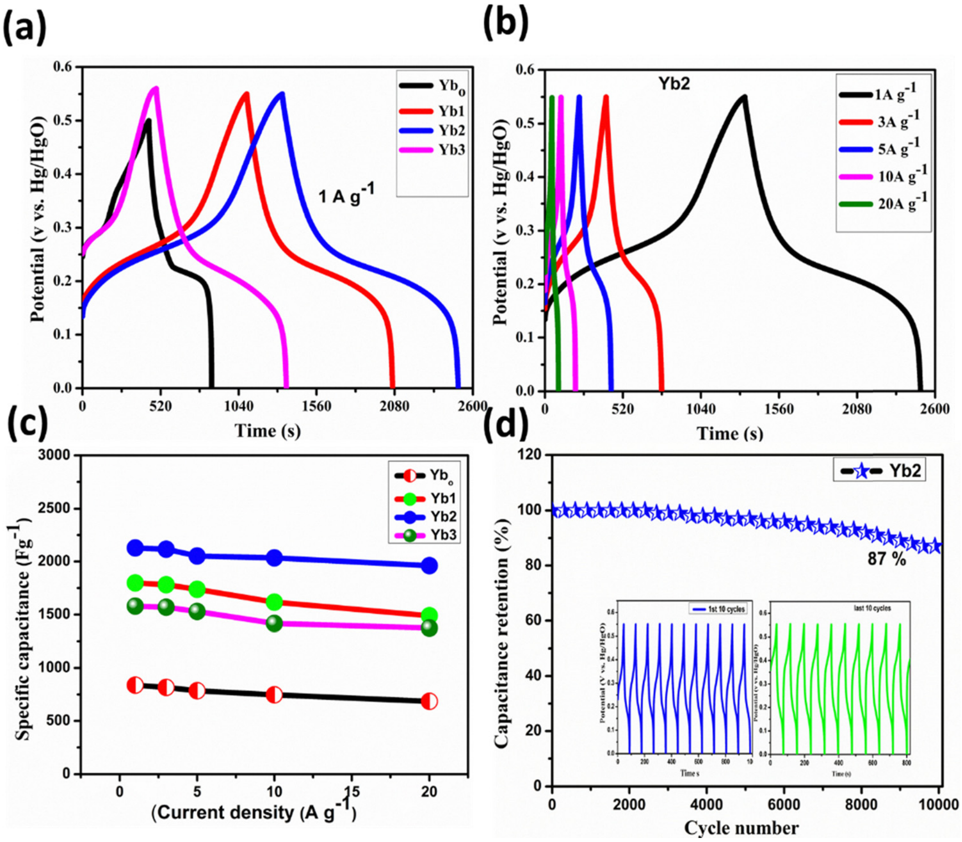

Fig. 7 (a) GCD data of Yb_0, Yb_1, Yb_2, and Yb_3, and (b) GCD profile for Yb_2. (c) Evaluation of specific capacitance with current density for Yb_0, Yb_1, Yb_2, and Yb_3, and (d) cyclic stability of Yb_2.

suggests strong suitability of the electrode material for supercapacitor applications.

$$I(\nu) = k_1\nu + k_2\nu^{1/2}. \quad (9)$$

$$I(\nu)\ \nu^{1/2} = k\nu^{1/2} + k_2 \quad (10)$$

Additionally, further insight into the charge-transfer characteristics of the electrode materials was gained from electrochemical impedance spectroscopy. Fig. 6f displays the Nyquist plots with fitted circuits, where a high-frequency semicircle and a low-frequency linear region are observed; the semicircle diameter corresponds to the charge transfer resistance (R_{ct}), while the low-frequency intercept reflects the solution resistance (R_s), implying that redox processes occur within the material. The steeper low-frequency slope (W_o) points to more rapid ion diffusion in the electrode. Yb_2 demonstrates a larger slope relative to the other materials, denoting enhanced electrical conductivity. The constant phase element (CPE) represents the interfacial resistance at the electrode–electrolyte boundary.[46,47] The R_s and R_{ct} values for all materials, listed in Table 3, indicate that Yb_2 has the smallest R_s and R_{ct} values, signaling faster faradaic reaction and superior energy storage capability.

The electrochemical characteristics were further probed *via* GCD, with the comparative profiles of all synthesized nanocomposites at a current density of 1 A g^{-1} presented in Fig. 7a. The Yb_2 sample exhibits a significantly larger GCD enclosed area, indicative of a greater charge storage capacity relative to its counterparts. Laterally, this feature is attributed to its highly ordered porous framework, which promotes more efficient ion transport than randomly arranged pores in the other sheets. The rate capability of the Yb_2 electrode is demonstrated by its GCD curves at different current densities, as displayed in Fig. 7b. GCD analysis of Yb_0, Yb_1, and Yb_3 (Fig. S3, SI) revealed non-linear but highly symmetrical profiles, consistent with diffusion-controlled faradaic processes at the electrode–electrolyte interface. Using eqn (1), the specific capacitances were determined to be 838, 1800, 2130, and 1581 F g^{-1} for Yb_0, Yb_1, Yb_2, and Yb_3 at 1 A g^{-1}, respectively. Among the samples, Yb_2 delivers the highest capacitance, attributable to its high specific surface area and meticulously ordered porosity, as evidenced by the data in Fig. 7c. The cyclic stability of the Yb_2 electrode, which was tested in over 10 000 cycles, exhibited a capacitance retention of 87% at 20 A g^{-1}. The cyclic durability of the Yb_2 electrode is further confirmed in the inset of Fig. 7d, which shows the near-identical shapes of the initial and final ten GCD cycles, indicating excellent long-term stability.

To further elucidate the energy storage mechanism of the synthesized material, an ASC device was assembled by pairing Yb_2 as the positive electrode with AC as the negative electrode in a 2 M KOH electrolyte. A comprehensive set of tests, including CV, GCD, EIS, and cycling stability, was performed. Fig. 8a shows the CV curves for Yb_2 and AC electrodes recorded at 50 mV s^{-1} with potential windows of 0–0.9 V for Yb_2 and 0–0.6 V for AC, revealing

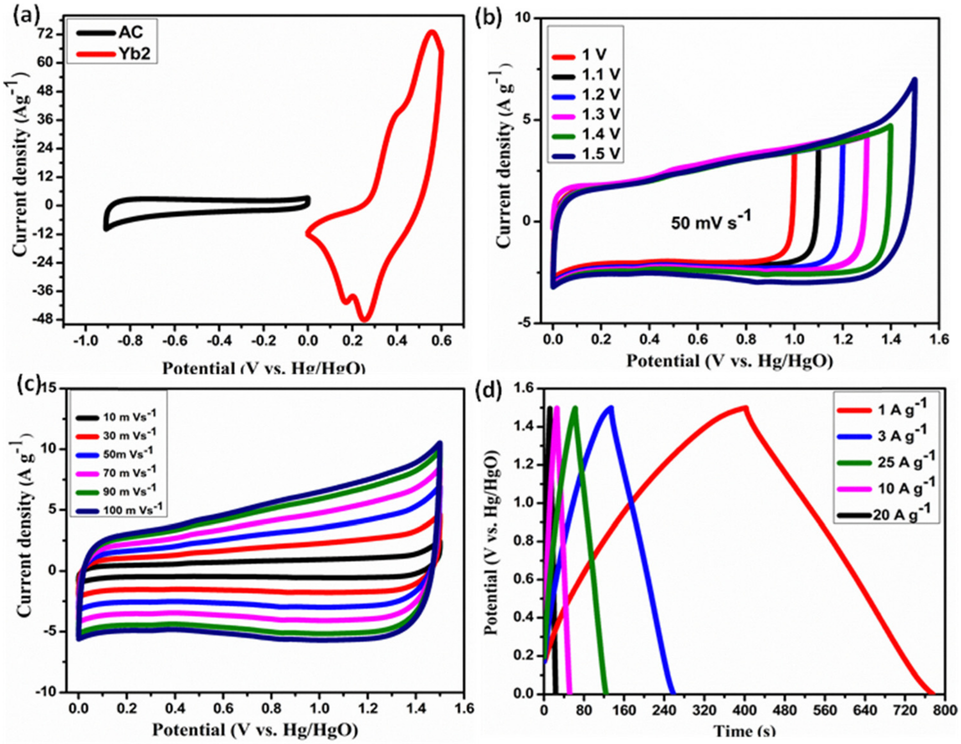

Fig. 8 Electrochemical characterization of ASC. (a) CV curves of the cathode (Yb_2) and anode (AC carbon) materials. (b) CV profile of the assembled ASC device at 50 mV s^{-1} with varying potential windows. (c) CV curve of the ASC device at scan rates ranging from 10 mV s^{-1} to 100 mV s^{-1}. (d) GCD curves of the ASC device at current densities of 1 A g^{-1} to 20 A g^{-1}.

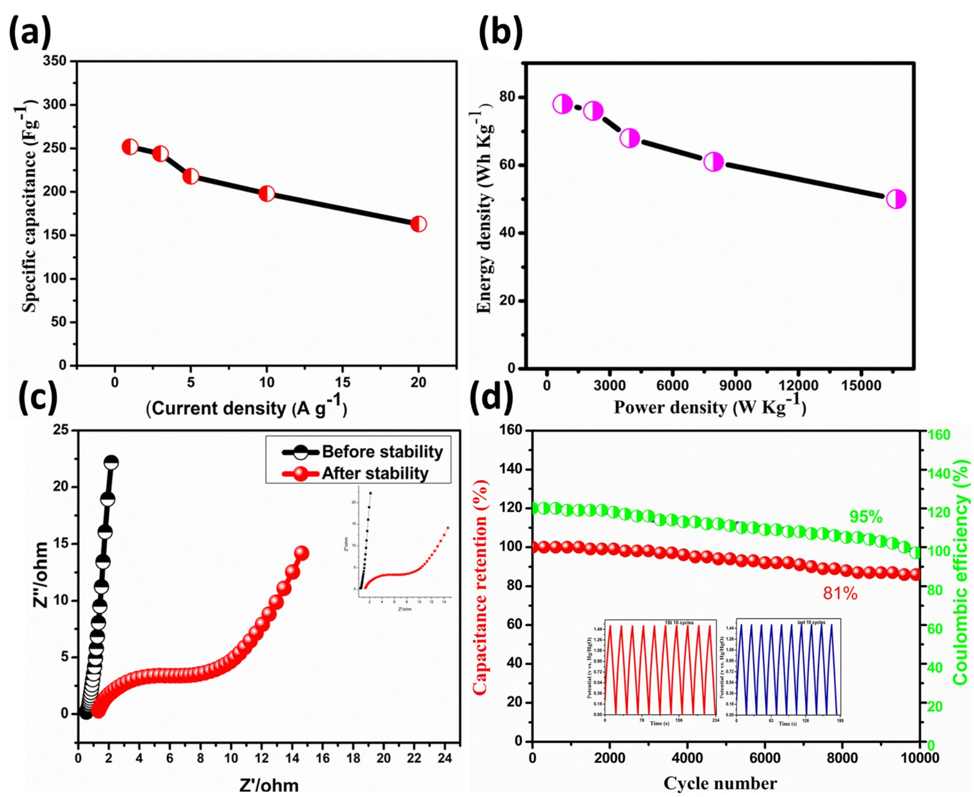

Fig. 9 (a) Specific capacitance *versus* charge–discharge current, (b) Ragone plot, (c) Nyquist plot, and (d) cyclic stability at 20 A g^{-1} of the ASC device.

pseudo-capacitance behavior for Yb_2 and a primarily EDLC behavior for AC. To establish a stable operational voltage, CV tests across a range of voltages show negligible polarization up to 1.5 V, establishing 1.5 V as the stable operating window. The quasi-rectangular shape of the CV curves (Fig. 8c) acquired at various scan rates within the 0–1.5 V range, exhibiting near-ideal capacitive, quasi-triangular shapes. Furthermore, the GCD curves obtained at different current densities show symmetric profiles, consistent with the CV results (Fig. 8d).

Fig. 9a presents the calculated specific capacitance of the ASC device at various current densities, yielding values of 252, 244, 218, 158, and 163 F g^{-1} from 1 to 20 A g^{-1}, with a mass loading of 6.20 mg. Likewise, eqn (2) and (3) were employed to determine the energy and power densities, yielding an energy density of 78 Wh kg^{-1} at a power density of 751 W kg^{-1}, as shown in Fig. 9b. EIS measurements were conducted before and after the cycling stability test, with initial R_s and R_{ct} values of 0.48 Ω and 0.68 Ω, respectively, and post-stability test values of R_s and R_{ct} of 1.29 Ω and 3.91 Ω, indicating a slight rise in resistance due to minor degradation of the materials and a reduction in conductivity. To evaluate durability, the ASC device was subjected to 10 000 charge–discharge cycles, retaining 81% of its original capacitance and 95% of its Coulombic efficiency. The inset of Fig. 9d compares the first and last ten cycles, which are nearly superimposable, affirming the robust stability of the ASC device, attributed to the high porosity and large surface area of the Yb_2 material.

4. Conclusion

In this study, Yb/NiCo-LDH nanocomposites were successfully synthesized through a simple hydrothermal approach with varying concentrations of Yb dopant. The introduction of Yb ions effectively modified the morphology, resulting in well-developed porous nanosheets with a large surface area. These structural features created additional channels for ion diffusion and electron transport, significantly improving the electrochemical performance. Among the prepared samples, the Yb_2 nanocomposite exhibited the best results, achieving a high specific capacitance of 2130 F g^{-1} at a current density of 1 A g^{-1}. The asymmetric supercapacitor (ASC) device assembled using Yb_2 as the positive electrode and activated carbon as the negative electrode demonstrated excellent energy storage capability. It delivered an energy density of 78 Wh kg^{-1} and a power density of 751 W kg^{-1}, maintaining 81% capacitance retention even after 10 000 charge–discharge cycles. This outstanding cyclic stability confirms the robustness and reversibility of the redox reactions occurring within the electrode. Overall, the superior electrochemical behavior of Yb_2 can be attributed to its optimized Yb doping level, high electrical conductivity, abundant active sites, and well-organized pore network. These results indicate that the Yb/NiCo-LDH nanocomposite is a promising electrode material for high-performance supercapacitor applications, offering both high energy density and long-term stability that is suitable for future energy storage devices.

Conflicts of interest

There are no conflicts to declare.

Data availability

The data supporting the findings of this study are available within the article and its supplementary information (SI). Additional datasets generated and analyzed during the current work are available from the corresponding author upon reasonable request. Supplementary information is available. See DOI: https://doi.org/10.1039/d5tc04078g.

Acknowledgements

The authors express their gratitude to the support from the Princess Nourah bint Abdulrahman University Researchers Supporting Project (PNURSP2026R58), Princess Nourah bint Abdulrahman University, Riyadh, Saudi Arabia.

References

1 H. Liu, *et al.*, Fe_2O_3/N doped rGO anode hybridized with NiCo LDH/Co $(OH)_2$ cathode for battery-like supercapacitor, *Chem. Eng. J.*, 2021, **403**, 126325.
2 H. Liu, *et al.*, Porous V_2O_5 nanorods/reduced graphene oxide composites for high performance symmetric supercapacitors, *Appl. Surf. Sci.*, 2019, **478**, 383–392.
3 Y. Yuan, *et al.*, Fe substitution in urchin-like $NiCo_2O_4$ for energy storage devices, *RSC Adv.*, 2019, **9**(13), 7210–7217.
4 Y. Yuan, *et al.*, Two-step method for synthesizing polyaniline with bimodal nanostructures for high performance supercapacitors, *Electrochim. Acta*, 2018, **282**, 286–294.
5 B. Zhang, *et al.*, Facile gravity-steered fabrication of free-standing bilayer composite films for flexible micro-supercapacitor enhancement, *J. Alloys Compd.*, 2025, 182003.
6 M. U. Khan, *et al.*, Controlled phase engineering of electrochemically reconstructed MnO_2-SnSe|| AC asymmetrical electrode with enhanced charge storage capability for supercapacitor, *Electrochim. Acta*, 2025, **537**, 146867.
7 L. Hou, *et al.*, Self-reconstruction strategy to synthesis of Ni/Co-OOH nanoflowers decorated with N, S co-doped carbon for high-performance energy storage, *Chem. Eng. J.*, 2020, **396**, 125323.
8 S. Ahmad, *et al.*, Engineering 3D Delhi flower-like ZIF-67 derived NiCo layer double hydroxide electrodes with vertically aligned channels for high performance supercapacitor, *Electrochim. Acta*, 2025, 147517.
9 C. Yang, *et al.*, Three-dimensional independent CoZnAl-LDH nanosheets via asymmetric etching of Zn/Al dual ions for high-performance supercapacitors, *J. Alloys Compd.*, 2021, **861**, 157933.

10 Z. Zhu, F. Cai and J. Yu, Improvement of electrochemical performance for AlF_3-coated $Li_{1.3}Mn_{4/6}Ni_{1/6}Co_{1/6}O_{2.40}$ cathode materials for Li-ion batteries, *Ionics*, 2016, **22**(8), 1353–1359.

11 M. Zhang, *et al.*, A dual-modification strategy for both the Quinone-based cathode and Zn anode electrodes of the aqueous zinc-ion battery, *Chem. Eng. J.*, 2025, **511**, 161944.

12 A. U. Khan, *et al.*, A facile synthesis of novel binder-free NiSe-SnSe electrode: With enhanced electrochemical performance and superior life span, *J. Energy Storage*, 2024, **91**, 112068.

13 T. Wang, *et al.*, 2-Methylimidazole-derived Ni–Co layered double hydroxide nanosheets as high rate capability and high energy density storage material in hybrid supercapacitors, *ACS Appl. Mater. Interfaces*, 2017, **9**(18), 15510–15524.

14 Y. Wen, *et al.*, *Facile synthesis of ultrathin $NiCo_2S_4$ nanopetals inspired by blooming buds for high-performance supercapacitors, 2017.*

15 Z. Wu, *et al.*, Vanadium doped hierarchical porous nickel-cobalt layered double hydroxides nanosheet arrays for high-performance supercapacitor, *J. Alloys Compd.*, 2020, **838**, 155604.

16 Y. Liu, *et al.*, Reduced $CoNi_2S_4$ nanosheets decorated by sulfur vacancies with enhanced electrochemical performance for asymmetric supercapacitors, *Sci. China Mater.*, 2020, **63**(7), 1216–1226.

17 X. Wang, *et al.*, Design and synthesis of ternary-component layered double hydroxides for high-performance supercapacitors: understanding the role of trivalent metal ions, *Electrochim. Acta*, 2017, **225**, 263–271.

18 M. Yi, *et al.*, Ionic liquid-assisted synthesis of N, F, and B co-doped BiOBr/Bi2Se3 on Mo2CTx for enhanced performance in hydrogen evolution reaction and supercapacitors, *J. Colloid Interface Sci.*, 2024, **658**, 334–342.

19 S. Liu, *et al.*, 3D simulation and performance analysis of the non-isothermal charge/discharge processes in thermo-electrochemical cycle, *J. Power Sources*, 2026, **661**, 238695.

20 W. Zou, *et al.*, Anion Exchange of Ni–Co Layered Double Hydroxide (LDH) Nanoarrays for a High-Capacitance Supercapacitor Electrode: A Comparison of Alkali Anion Exchange and Sulfuration, *Chem. – Eur. J.*, 2018, **24**(72), 19309–19316.

21 L. Kang, *et al.*, Effect of fluorine doping and sulfur vacancies of CuCo2S4 on its electrochemical performance in supercapacitors, *Chem. Eng. J.*, 2020, **390**, 124643.

22 P. Sun, *et al.*, Uniform MoS2 nanolayer with sulfur vacancy on carbon nanotube networks as binder-free electrodes for asymmetrical supercapacitor, *Appl. Surf. Sci.*, 2019, **475**, 793–802.

23 S. Ahmad, *et al.*, A self-supporting Co (OH) F nanosquares with ion and electron conductive structure for high performance electrochemical energy storage, *J. Energy Storage*, 2025, **114**, 115816.

24 A. U. Khan, *et al.*, Advancements in the green synthesis of carbon dots for sustainable development, *Sustainable Mater. Technol.*, 2024, **41**, e01004.

25 H. Zhang, *et al.*, One-step hydrothermal synthesis of NiCo2S4 nanoplates/nitrogen-doped mesoporous carbon composites as advanced electrodes for asymmetric supercapacitors, *J. Power Sources*, 2019, **439**, 227082.

26 R. Li, *et al.*, NiCo2S4@ Co (OH) 2 core-shell nanotube arrays in situ grown on Ni foam for high performances asymmetric supercapacitors, *J. Power Sources*, 2016, **312**, 156–164.

27 X. Zhang, *et al.*, Nickel-cobalt double oxides with rich oxygen vacancies by B-doping for asymmetric supercapacitors with high energy densities, *Appl. Surf. Sci.*, 2020, **512**, 145621.

28 Y. Liu, *et al.*, Co-ZIF derived porous NiCo-LDH nanosheets/N doped carbon foam for high-performance supercapacitor, *Carbon*, 2020, **165**, 129–138.

29 H. Jin, *et al.*, Ni–Co layered double hydroxide on carbon nanorods and graphene nanoribbons derived from MOFs for supercapacitors, *Dalton Trans.*, 2018, **47**(26), 8706–8715.

30 Y. Dai, *et al.*, Synergistic coupling of NiCo-LDH in high-performance supercapacitors via hydrothermal method: Optimal utilization of the potential window, *J. Alloys Compd.*, 2025, **1010**, 177091.

31 A. U. Khan, *et al.*, Constructing strain and defects modulated novel germanium doped zeolitic imidazolate framework-67 derived NiCo layer double hydroxide nanocomposites for boosted supercapacitor applications, *J. Energy Storage*, 2025, **134**, 118193.

32 E. Samuel, *et al.*, Supersonically sprayed Zn2SnO4/SnO2/CNT nanocomposites for high-performance supercapacitor electrodes, *ACS Sustainable Chem. Eng.*, 2019, **7**(16), 14031–14040.

33 Y. Zhang, *et al.*, Self-assembled Cobalt-doped NiMn-layered double hydroxide (LDH)/V2CTx MXene hybrids for advanced aqueous electrochemical energy storage properties, *Chem. Eng. J.*, 2022, **430**, 132992.

34 J. Wang, *et al.*, Enhanced ordered growth of NiCo LDH nanosheets on N-doped carbon through nitrogen configuration tuning for high-performance asymmetric supercapacitors, *J. Energy Storage*, 2024, **98**, 113180.

35 L. Xu, *et al.*, Mo-doped NiCo-LDH nanoflower derived from ZIF-67 nanosheet arrays for high-performance supercapacitors, *J. Energy Storage*, 2024, **77**, 109781.

36 Z. Xu, *et al.*, Mn-doped NiCo LDH nanosheets with rich oxygen vacancies for high-performance supercapacitors and efficient oxygen evolution, *J. Energy Storage*, 2025, **106**, 114848.

37 Z. Shi, *et al.*, Sulfur-doped nickel–cobalt double hydroxide electrodes for high-performance asymmetric supercapacitors, *ACS Appl. Energy Mater.*, 2020, **3**(11), 11082–11090.

38 G. Kim, *et al.*, A Systematic Study of NiCo Layered Double Hydroxides Grown on Porous Carbon for Hybrid Battery-like Supercapacitor Electrodes: Growth Method, Morphology, and Composition, *ACS Appl. Energy Mater.*, 2024, **7**(18), 8085–8097.

39 J. Rouquerol, *et al.*, Recommendations for the characterization of porous solids (Technical Report), *Pure Appl. Chem.*, 1994, **66**(8), 1739–1758.

40 C. Dang, *et al.*, Direct dissolution of cellulose in NaOH/urea/α-lipoic acid aqueous solution to fabricate all biomass-based nitrogen, sulfur dual-doped hierarchical porous carbon aerogels for supercapacitors, *ACS Appl. Mater. Interfaces*, 2020, **12**(19), 21528–21538.

41 T. Guo, *et al.*, Controllable synthesis of ultrathin defect-rich LDH Nanoarrays coupled with MOF-derived Co-NC microarrays for efficient overall water splitting, *Small*, 2022, **18**(29), 2107739.

42 X. Jiang, *et al.*, The synthesis and characterization of ytterbium-doped TiO 2 hollow spheres with enhanced visible-light photocatalytic activity, *RSC Adv.*, 2017, **7**(40), 24598–24606.

43 H. Li, *et al.*, Amorphous nickel hydroxide nanospheres with ultrahigh capacitance and energy density as electrochemical pseudocapacitor materials, *Nat. Commun.*, 2013, **4**(1), 1894.

44 T. Dong, *et al.*, Hierarchical flower-like Ni–Co layered double hydroxide nanostructures: synthesis and super performance, *Inorg. Chem. Front.*, 2018, **5**(12), 3033–3041.

45 S. Ahmad, *et al.*, Constructing Fluorine modified NiCo-LDH nanocomposite for enhanced supercapacitor performance through active site and structural optimization, *Electrochim. Acta*, 2025, **532**, 146452.

46 L. Su, *et al.*, Orderly Arranged Bead-Chain Cu2O-Mn3O4-NiO Ternary Nanocomposites with High Specific Capacitance for Supercapacitors, *Nano*, 2020, **15**(06), 2050082.

47 R. Zou, *et al.*, Arginine-assisted thermal decomposition for synthesis of nanosized Co3O4 with enhanced capacitance, *Int. J. Electrochem. Sci.*, 2020, **15**(1), 484–492.